CFA-2 and CFA-3 (Coordination Framework Augsburg University-2 and -3); novel MOFs assembled from trinuclear Cu(I)/Ag(I) secondary building units and 3,3′,5,5′-tetraphenyl-bipyrazolate ligands†

Maciej Grzywa,[a,b] Christof Geßner,[b] Dmytro Denysenko,[a] Björn Bredenkötter,[a] Fabienne Gschwind,[c] Katharina M. Fromm,[c] Wojciech Nitek,[d] Elias Klemm[b] and Dirk Volkmer*[a]

The syntheses of H_2-phbpz, [Cu_2(phbpz)]·2DEF·MeOH (**CFA-2**) and [Ag_2(phbpz)] (**CFA-3**) (H_2-phbpz = 3,3′,5,5′-tetraphenyl-1*H*,1′*H*-4,4′-bipyrazole) compounds and their crystal structures are described. The Cu(I) containing metal–organic framework **CFA-2** crystallizes in the tetragonal crystal system, within space group $I4_1/a$ (no. 88) and the following unit cell parameters: a = 30.835(14), c = 29.306(7) Å, V = 27 865(19) Å^3. **CFA-2** features a flexible 3-D three-connected two-fold interpenetrated porous structure constructed of triangular Cu(I) subunits. Upon exposure to different kinds of liquids (MeOH, EtOH, DMF, DEF) **CFA-2** shows pronounced breathing effects. **CFA-3** crystallizes in the monoclinic crystal system, within space group $P2_1/c$ (no. 14) and the following unit cell parameters: a = 16.3399(3), b = 32.7506(4), c = 16.2624(3) Å, β = 107.382(2)°, V = 8305.3(2) Å^3. In contrast to the former compound, **CFA-3** features a layered 2-D three-connected structure constructed from triangular Ag(I) subunits. Both compounds are characterized by elemental and thermogravimetric analyses, single crystal structure analysis and X-ray powder diffraction, FTIR- and fluorescence spectroscopy. Preliminary results on oxygen activation in **CFA-2** are presented and potential improvements in terms of framework robustness and catalytic efficiency are discussed.

Introduction

Porous coordination polymers, often referred to as metal–organic frameworks (MOFs), have been extensively studied during the past decade owing to their fascinating crystal structures, variety of bonding topologies as well as for their wide range of applications including gas storage[1] and separation,[2] controlled drug release,[3] sensing,[4] or catalysis.[5] Heterogeneous catalysis has recently shifted into the focus of research because MOF compounds can be rationally designed, bearing uniform catalytically active sites at high volume densities.[6] The building block approach offers the possibility to program multifunctionality into these materials, while their spontaneous self-assembly from ligands and metal ions fulfills the needs of an economical fabrication. Most notably, homochiral MOFs can be prepared, which opens up novel possibilities for chiral enantioselective (catalytic) transformations.[7]

Among the many metal ions demonstrated as useful in catalysis, investigations on copper-containing MOFs bear great potential with respect to the activation of molecular oxygen at close-to-ambient conditions, which is reflected in the occurrence of (multi-)copper active sites in natural enzymes, such as oxidases or oxygenases.[8] Biologically inspired MOF catalysts trying to mimic structural and functional aspects of these enzymes hold great promise for wide-ranging synthetic applications in the oxidation of organic intermediates containing non-activated C–H-bonds. However, the use of Cu-MOFs as catalysts at a commercial production scale is still in its infancy, because few MOF compounds currently fulfill the stringent requirements of high catalytic activity and selectivity, paired

[a]*Institute of Physics, Chair of Solid State and Materials Chemistry, Augsburg University, Universitätsstrasse 1, D-86159 Augsburg, Germany. E-mail: dirk.volkmer@physik.uni-augsburg.de; Fax: +49 (0) 821 598-5955; Tel: +49 (0) 821 598-3006*

[b]*Institute of Chemical Technology, Faculty of Chemistry, University of Stuttgart, Pfaffenwaldring 55, D-70569 Stuttgart, Germany*

[c]*Department of Chemistry, University of Fribourg, Chemin du Musée 9, 1700 Fribourg, Switzerland*

[d]*Faculty of Chemistry, Jagiellonian University, ul. Ingardena 3, 30-060 Kraków, Poland*

†Electronic supplementary information (ESI) available: Atomic coordinates, bond lengths and angles, asymmetric units for **1**, **CFA-2** and **CFA-3**, XRPD patterns, SEM picture, IR, ^{1}H NMR and ^{13}C NMR spectra. CCDC 903114–903116. For ESI and crystallographic data in CIF or other electronic format see DOI: 10.1039/c3dt32302a

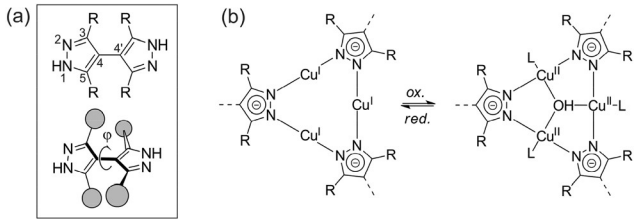

Scheme 1 (a) Ligand (3,3′,5,5′-tetraphenyl-1*H*,1′*H*-4,4′-bipyrazole, R = Ph) employed in the current work. (b) Secondary building unit of Cu(I)-containing frameworks and their redox transformation into trinuclear Cu(II) units (L = monodentate neutral or anionic ligand).

with long-term stability. Until now, there are only a few reports appearing in the literature where Cu-MOFs have been studied and applied as oxidation catalysts. In particular, Cu-catalyzed hydroxylation of phenol,[9] oxidation of trimethylsilyl enolates to α-hydroxy ketones,[10] allylic oxidation of cyclohexene,[11] oxidation of benzene derivatives and tetralin have been described.[12,13] Here, we report on the development of copper-based MOFs containing triangular Cu(I) subunits that are linked by bipyrazolate ligands and we provide first insights into their use in oxidation catalysis (Scheme 1). The exploration of this particular type of MOF compound has the following rationales: first, polyaza-heteroaromatic ligands such as pyrazole, imidazole, triazole, tetrazole, *etc.* have emerged as useful ligands in constructing robust coordination polymers (MAFs – metal azolate frameworks) providing superior chemical and thermal stability as compared to their widespread carboxylate-based counterparts.[14] In order to construct a three-dimensional framework we have employed the tetradentate 3,3′,5,5′-tetraphenyl-4,4′-bipyrazolate ligand (Scheme 1), which in its deprotonated state can bind up to four metal ions.

Monovalent precious metal ions (Cu^{I}, Ag^{I}, Au^{I}, d^{10} electron configuration), when combined with pyrazolate ligands, quite often form planar trinuclear coordination compounds,[15] which also have been introduced as secondary building units (SBUs) into metal–organic frameworks.[16] In particular, coordination compounds or MOFs containing linear (two-fold) coordinated Cu(I) centers show distinct redox behaviour which upon oxidation leads to oxygen-centered trinuclear coordination units comprising Cu(II) centers with a square planar coordination geometry (Scheme 1). This chemical transformation occurs with minimal structural distortion of the trinuclear SBU. Therefore, the low coordination number of the Cu(I)/Cu(II) sites as well as their high accessibility should render MOFs comprising this particular SBU attractive candidates for oxygen activation and redox catalysis. However, the exact reaction pathway by which oxygen molecules might bind to the Cu(I) centers in these trinuclear coordination units as yet is largely unknown. Recent investigations of the Chan group[17] reveal that mixing $[Cu^{I}Cu^{I}Cu^{I}(L)]^{1+}$ (L = 3,3′-(1,4-diazepane-1,4-diyl)bis(1-{[2-(dimethylamino)-ethyl](methyl)amino}propan-2-ol) or 3,3′-(1,4-diazepane-1,4-diyl)bis-(1-{[2-(diethylamino)-ethyl](ethyl)-amino}propan-2-ol)) with O_2-saturated propionitrile (EtCN) led to species $[Cu^{II}Cu^{II}(\mu\text{–}\eta^2\text{:}\eta^2\text{-peroxo})Cu^{II}(L)]^{2+}$ and $[Cu^{II}Cu^{II}(\mu\text{-O})Cu^{II}(L)]^{2+}$. Moreover, all literature-known coordination frameworks containing trinuclear M^{I} coordination units and bipyrazolate linkers are structurally highly flexible, leading to strong geometric lattice distortions upon removal or exchange of clathrated molecules. While this "breathing effect" might be advantageous in gas separation or sensing applications,[18] it represents a less desirable feature in heterogeneous catalysis. Aiming at robust catalysts, back-to-back bonded (linear) bipyrazole ligands in particular offer many possibilities for a rational crystal design due to their ease of synthesis, and structural adaptability. In the present study we are exploring the influence of large substituents (Scheme 1, R = phenyl) on the 3D structure of MOFs featuring planar trinuclear M^{I} SBUs, where the most important geometric parameter is represented by the torsion angle φ between the planar heterocyclic ring systems of the bipyrazole ligand which coincides with the torsion angle between adjacent trinuclear SBUs, respectively.

Results and discussion

Syntheses and characterization

The 3,3′,5,5′-tetraphenyl-1*H*,1′*H*-4,4′-bipyrazole ligand (**1**) was synthesized by a modified published procedure.[19] Compound **CFA-2** was obtained as colorless crystals (Fig. 1) after heating a DEF–MeOH solution of 3,3′,5,5′-tetraphenyl-1*H*,1′*H*-4,4′-bipyrazole (**1**) and copper(II) acetate monohydrate in the presence of Et_3N. The addition of amine is necessary in order to deprotonate the ligand. A small amount of water impurity in the synthesis causes precipitation of amorphous material and no formation of **CFA-2**. Besides the solvothermal synthesis, an alternative route *via* diffusion precipitation was developed. **CFA-3** was obtained *via* diffusion synthesis by layering a solution of **1** in EtOH on top of an ammonia solution containing silver ions.

Single crystal structure analyses

3,3′,5,5′-Tetraphenyl-1*H*,1′*H*-4,4′-bipyrazole·DMSO ($C_{30}H_{22}N_4\cdot(CH_3)_2SO$) (1). Compound **1** crystallizes in the monoclinic crystal system within space group $P2_1/n$ (no. 14). The asymmetric unit consists of thirty carbon and four nitrogen atoms creating the whole independent molecule of 3,3′,5,5′-tetraphenyl-1*H*,1′*H*-4,4′-bipyrazole and the highly disordered DMSO (solvent) molecule (ESI, Fig. S1†). The pyrazole rings are inclined with respect to each other. The two equatorial planes

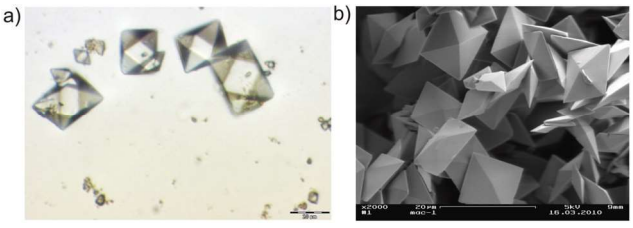

Fig. 1 (a) Optical micrograph and (b) SEM image of **CFA-2**.

created by N1, N2, C7–C9 and N3, N4, C22–C24 atoms enclose an angle of 87.60(4)°. The phenyl rings do not form a common plane with the pyrazole rings to which they are bound. The least-squares planes defined by the pyrazole ring (N1, N2, C7–C9) and phenyl ring 1 (C1–C6), and phenyl ring 2 (C10–C15), enclose angles of 9.3(1) and 52.99(6)°, respectively. Similar torsion angles (12.0(1) and 43.37(8)°) are found for the phenyl ring system 3 (C16–C21), and 4 (C25–C31), bound to the parent pyrazole ring (N3, N4, C22–C24) (*cf.* Fig. S1†). An Ortep style plot of the asymmetric unit of **1** with the atom labels is shown in the ESI, Fig. S1.† A packing diagram of **1** is shown in Fig. 2. The atomic coordinates, isotropic thermal parameters, selected bond lengths and angles for **1** are given in Tables S1 and S2 (ESI†), respectively.

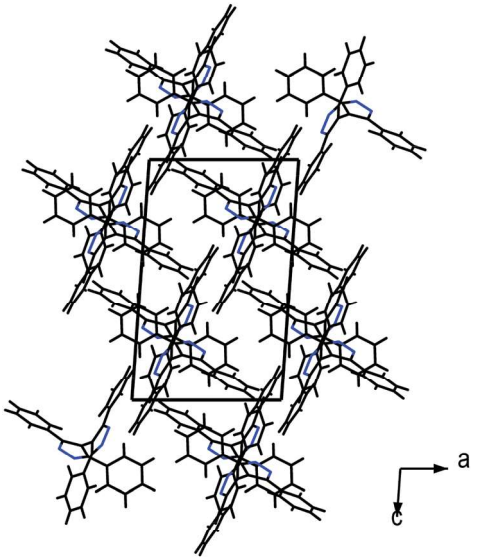

Fig. 2 Packing of 3,3′,5,5′-tetraphenyl-1*H*,1′*H*-4,4′-bipyrazole molecules in the crystal lattice of (**1**); view in the *b*-direction. The disordered DMSO molecules were omitted for clarity.

[Cu$_2$(phbpz)]·2DEF·MeOH (CFA-2). **CFA-2** crystallizes in the tetragonal crystal system in the space group $I4_1/a$ (no. 88). The asymmetric unit consists of forty-five carbon, six nitrogen and three copper atoms. An Ortep style plot of the asymmetric unit of **CFA-2** with atom labels is shown in the ESI, Fig. S2.† [Cu$_2$(phbpz)]·2DEF·MeOH features an extended 3-D two-fold interpenetrated porous structure constructed from triangular secondary building units, each containing a trinuclear coordination unit of Cu(I) ions and three pyrazolate ligands, as shown in Fig. 3a. The Cu(I) ions within each SBU are almost linearly coordinated by two nitrogen donors stemming from adjacent ligand molecules; the N–Cu–N dihedral angles therefore are close to 180° (173.04(8), 177.78(8), and 174.02(8)°). The Cu ions are bridged by three pyrazolates to form almost planar triangles, a coordination motif which is frequently observed in low-valent metal pyrazolates, pyridinates and amidinates.[15,16] The Cu–N distances range from 1.849(2) to 1.863(2) Å. The Cu(2) and Cu(3) atoms are shifted outwards by −0.2214(8) and 0.2078(8) Å, respectively, from the Cu_3N_6 plane. The biggest displacement from the Cu_3N_6 plane is observed for the N(1) atom (0.278(1) Å). The intratriangular Cu···Cu distances range from 3.192(2) to 3.263(1) Å and are in good agreement with the literature data.[15,16] The closest distance between copper atoms from two adjacent, separate triangles is equal to 7.651(3) Å, while the closest distance between two Cu_3 centroids is 9.603(3) Å. The pyrazole rings of each bipyrazolate linker are twisted with respect to each other, which is enforced by the strong steric repulsion between their phenyl substituents. An extensive π–π stacking of parallel and perpendicular-displaced phenyl rings belonging to bipyrazolate linkers is observed in the crystal packing arrangement of **CFA-2** (av. distances between geometric centers of phenyl rings and between geometric centers and H-atoms belonging to the neighbouring Ph-group: 3.0597(6)–4.1512(9) Å), which is

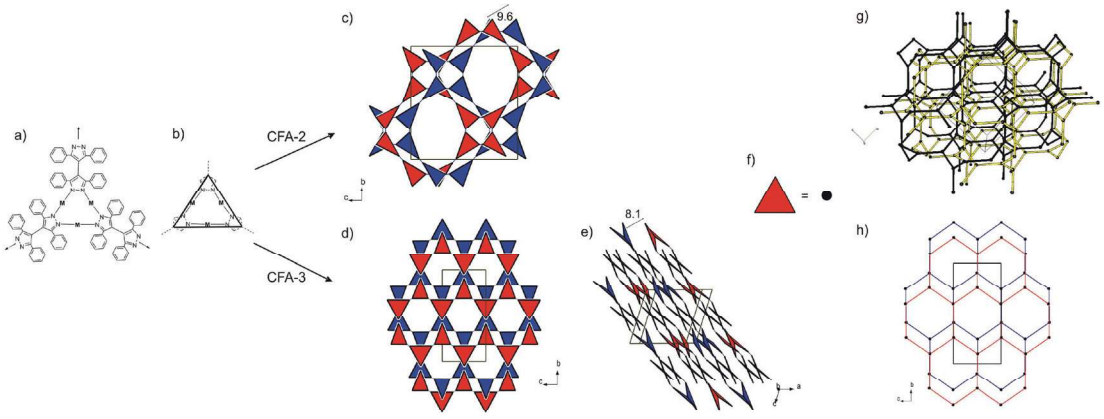

Fig. 3 (a) Coordination units of a M = Cu/Ag-containing framework featuring trinuclear Cu(I)/Ag(I) centres. (b) Simplified diagram of SBUs (Ph-groups of the 3,3′,5,5′-tetraphenyl-1*H*,1′*H*-4,4-bipyrazole ligand (phbpz) omitted for clarity). (c) Packing diagram represented by interconnected SBUs of **CFA-2** showing an interpenetrated porous 3D framework projected along the *a*-axis (solvent molecules omitted for clarity). (d) Packing diagram of SBUs of **CFA-3** projected along the *a*-axis (d) and *b*-axis (e). Simplified diagram of trinuclear $Cu(I)_3$ units (f). Topologic representation of **CFA-2** (g) and **CFA-3** (h) showing two-fold interpenetrated (10,3)-*a* coordination networks (**CFA-2**) and a (6,3) hexagonal plane net (**CFA-3**).

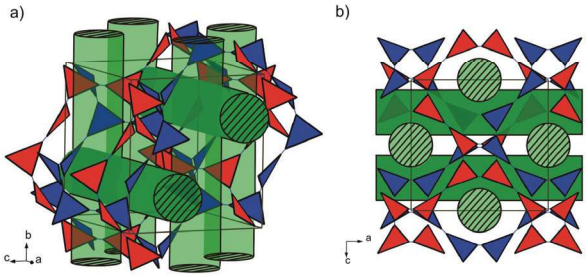

Fig. 4 Schematic packing diagrams of SBUs of **CFA-2** with channels, view in the *a*- (a) and *b*-direction (b).

responsible for stabilizing the crystal structure. The distortion of Cu_3-$(pz)_3$ SBUs from ideal trigonal planar geometry also contributes to the overall network distortion. In the first approximation the [Cu_2(phbpz)] coordination network (Fig. 3c) can be simplified by regarding each Cu_3-pz_3 SBU as a triangle (Fig. 3b). These SBUs are interconnected by single bonds, allowing for an (almost) unconstrained rotation. Next, the **CFA-2** coordination network can be described as a network comprising (10,3)-*a* topology (type srs, $SrSi_2$) by regarding the $Cu_3(pz)_3$ SBUs as three-connected nodes and the $phbpz^{2-}$ ligands as spacers of length 10.501(6)–10.677(7) Å (see Fig. 3f and g). The packing diagram of **CFA-2** depicted in Fig. 4 shows 2D hydrophobic channels along the [100] and [010] directions flanked by hydrogen atoms stemming from phenyl groups of the ligands. The size-limiting feature of these channels are tubes centered at *x*, 0.75, 0.25 and *x*, 0.25, 0.75 (along [100]), 0.5, *y*, 0, 0.5, *y*, 1, 0, *y*, 0.5 and 1, *y*, 0.5 (along [010]) with a radius defined by the distances between hydrogen atoms of the phenyl groups. Taking the van der Waals radii into account, the largest diameter of the channel is 14.564(7) Å but the smaller aperture of the channels may only admit the passage of a sphere with a diameter of approximately 7.0 Å. The wall of each tube consists of two alternating rings formed by ten trinuclear Cu-units connected together by $phbpz^{2-}$ ligands. The atomic coordinates and isotropic thermal parameters, selected bond lengths and angles for **CFA-2** are presented in the ESI, Tables S3 and S4,† respectively.

[Ag_2(phbpz)] (CFA-3). **CFA-3** crystallizes in the monoclinic space group $P2_1/c$ (no. 14). The asymmetric unit is created by six silver, twelve nitrogen and ninety carbon atoms. An Ortep style plot of the asymmetric unit of **CFA-3** with atom labels is shown in Fig. S3.† [Ag_2(phbpz)] features an extended 2-D porous structure constructed of triangular Ag(I) subunits shown in Fig. 3a. According to the calculations performed by the PLATON/SQUEEZE program[20] the initial total potentially accessible void volume of **CFA-3** is 497.2 $Å^3$ which is 6% of the unit cell volume (8305.3(2) $Å^3$). Packing diagrams of SBUs of **CFA-3** in the *a*- and *b*-direction are shown in Fig. 3d–e, respectively.

Three metal atoms, Ag_3, bridged through nitrogen atoms from pyrazolate groups form slightly puckered nine-membered rings Ag_3N_6 which are next connected together in planes parallel to the (10$\bar{1}$) plane. The intratriangle Ag···Ag distances range from 3.3088(6) to 3.7034(1) Å and are in good agreement with literature data.[16,21] Within the unequilateral two triangles Ag_3N_6 (asymmetric unit), the N–Ag–N angles deviate from linearity and range from 172.5(2) to 174.1(2) (Ag_3(1–3)) and from 170.9(2) to 177.7(2) (Ag_3(4–6)), respectively.

Two triangular units {Ag_3} from the neighbouring layers are well separated from each other. The closest distance between silver atoms from two neighbouring {Ag_3} units is equal to 6.8921(1) Å, while the closest distance between two {Ag_3} centroids is 8.135(1) Å. Two Ph-groups (C85–C90 and C57–C62) are disordered.

The crystal structure of **CFA-3** is stabilized by π–π stacking of parallel-displaced benzene rings, distances between centroids of aromatic rings range from 3.7212(1)–4.6617(1) Å. The coordination network of **CFA-3** can be simplified as a (6,3) topology (type hcb, Shubnikow hexagonal plane net) by considering the $Ag_3(pz)_3$ SBUs as three-connected nodes and the $phbpz^{2-}$ ligands as spacers of length 10.6543(1)–11.0901(2) Å (see Fig. 3f and h). The atomic coordinates and isotropic thermal parameters, selected bond lengths and angles for **CFA-3** are presented in the ESI in Tables S5 and S6,† respectively.

The advantage of the bipyrazole ligand with four bulky phenyl substituents in the MOF construction is that the degree of interpenetration decreases. In contrast to MOFs constructed from Me_4bpz ligands which exhibit eight- (β-M_2(Mebpz), Cu_2(Mebpz)) and four-fold (α-M_2(Mebpz), Ag_2(Mebpz)) interpenetration[16] **CFA-2** is two-fold interpenetrated. Framework flexibility of **CFA-2** results from the properties of the ph-bipyrazole ligand where two pyrazole rings can rotate around the central C–C single bond (φ). In **1** the pyrazole rings are almost perpendicular to each other (φ = 87.6°). The interplanar angles between triangle Cu_3-$(pz)_3$ units in **CFA-2**, **CFA-3** are 66.9(1)–77.5(1) and 27.2(2)–27.6(1), respectively, while in other coordination polymers based on the bipyrazole ligands the angles between moieties range from 7.5(3) to 74.5(3)°, see Table 1. No metallophilic (cupro- or argentophilic) interactions in **CFA-2** and **CFA-3**, respectively, are observed. The closest distances between {M_3} centroids are equal to 9.603(3) Å and 8.135(1) Å for **CFA-2** and **CFA-3**, respectively, which are significantly bigger than in other Cu-, Ag-bipyrazolate compounds listed in Table 1 (2.77(1)–4.29(1) Å).[16] In the case of **CFA-2** the {M_3} units are parallel and arranged at an angle of 62.2(3)° to each other. In other compounds the angles between least-squares M_3N_6 planes range from 0.0(1) to 7.8(2) and 57.6(2) to 86.6(2)°.[16]

TGA and XRPD studies

Microcrystalline powder samples of **CFA-2** can be handled in air for a longer time, and its color changes from white to light green after weeks reflecting very slow oxidation of Cu(I) to Cu(II). No color change is evident while **CFA-3** is exposed to ambient light for months reflecting the stability of Ag(I) in the framework. Phase purity of **CFA-2** was confirmed by an XRPD measurement with the sample kept at ambient conditions. The experimental XRPD pattern is consistent with the

Table 1 Structural data for **1** and Cu/Ag MOFs

Compound	Crystal system, space group	Unit cell parameters (Å) volume (Å^3)	Interplanar angle between triangle $Cu_3(pz)_3$ units (°)	The shortest distance between M_3 centroids (Å)	Net	Ref.
$C_{30}H_{22}N_4{\cdot}(CH_3)_2SO$	Monoclinic, $P2_1/n$	a = 10.3718(12) b = 16.0120(16) c = 16.776(2) β = 94.124(5) V = 2778.8(5)	—	—	—	Compound **1** (this work)
$Cu_2(C_{30}H_{20}N_4)$	Tetragonal, $I4_1/a$	a = 30.835(14) c = 29.306(7) V = 27 865(19)	66.9(1)–77.5(1)	9.603(3)	(10,3)-a,srs	**CFA-2** (this work)
$Ag_2(C_{30}H_{20}N_4)$	Monoclinic, $P2_1/c$	a = 16.3399(3) b = 32.7506(4) c = 16.2624(3) β = 107.38 V = 27491.3(12)	27.2(1)–27.6(1)	8.135(1)	(6,3) hcb	**CFA-3** (this work)
$(C_{60}H_{72}Cu_{12}N_{24})_n$	Orthorhombic, $Ccca$	a = 18.6363(13) b = 46.435(3) c = 34.874(3) V = 30 179(4)	10.2(3)–66.9(4)	4.29(1)	$(6^2 \times 10)(6 \times 10^2)$ nof	16
$(C_{60}H_{72}Cu_{12}N_{24})_n$	Orthorhombic, $Ccca$	a = 18.5370(19) b = 46.211(5) c = 34.925(4) V = 29 917(6)	7.5(3)–67.8(3)	3.91(2)	$(6^2 \times 10)(6 \times 10^2)$ nof	16
$(C_{150}H_{180}Ag_{30}N_{60})_n$, $8n(C_9H_{12})$	Tetragonal, $I4_1/a$	a = 61.7239(11) c = 26.9189(5) V = 10 2557	62.6(2)–72.7(3)	2.77(1)	(10,3)-a	16
$(C_{90}H_{108}Ag_{18}N_{36})_n$	Tetragonal, $I\bar{4}2d$	a = 27.1756(8) c = 81.019(3) V = 59 833(3)	68.3(3)–74.5(3)	3.02(3)	(10,3)-a	16
$(C_{60}H_{72}Ag_{12}N_{24})_n$	Orthorhombic, $Ccca$	a = 19.2056(5) b = 47.9669(16) c = 36.2063(9) V = 33 354(2)	62.5(2)–68.7(3)	3.51(1)	$(6^2 \times 10)(6 \times 10^2)$ nof	16
$(C_{150}H_{180}Ag_{30}N_{60})_n$, $10n(C_6H_6)$	Tetragonal, $I4_1/a$	a = 61.600(2) c = 26.7475(13) V = 101 495(7)	62.1(3)–70.6(3)	2.93(2)	(10,3)-a	16
$(C_{150}H_{180}Ag_{30}N_{60})_n$, $9n(C_7H_8)$	Tetragonal, $I4_1/a$	a = 62.030(2) c = 26.5872(15) V = 102 300(7)	62.9(3)–69.8(3)	2.96(2)	(10,3)-a	16
$C_{10}H_{12}Cu_2N_4$	Cubic, $I\bar{4}3d$	a = 26.407(3) V = 18 414(4)	70.5(2)	2.96(3)	(10,3)-a	16
$C_{10}H_{12}Ag_2N_4$	Cubic, $I\bar{4}3d$	a = 27.2326(15) V = 20 196(2)	70.5(2)	2.90(2)	(10,3)-a	16

simulated one as gleaned from the single-crystal X-ray diffraction data (Fig. 5). Differences in peak intensities are due to occluded solvent molecules.

In addition the thermal stability of $[Cu_2(phbpz)]{\cdot}2DEF{\cdot}MeOH$ (**CFA-2**) and $[Ag_2(phbpz)]$ (**CFA-3**) was determined by thermogravimetric (TG) and VTXRPD diffraction measurements. As shown in Fig. 6, under pure oxygen there is an initial weight loss of approximately 29% between 30–160 °C, corresponding to the loss of two molecules of DEF and one molecule of MeOH. The weight loss observed between 300–360 °C is attributed to the decomposition process accounting for 50.1% of the mass. This latter process is associated with the loss of the organic ligand. The final increase of mass is attributed to the oxidation of Cu_2O to CuO. Similar thermal behaviour was observed during heating of the MOF in a nitrogen atmosphere. There are also two decomposition steps. Notable exceptions are a first weight loss between 60–160 °C, 30.4% and a second weight-loss step occurring at much higher temperatures 540–1100 °C, 38.5%. Variable temperature powder X-ray diffraction (VTXRPD) studies show (Fig. 7) that $[Cu_2(phbpz)]$ is stable up to 240 °C in oxygen, 270 °C in air and up to 500 °C in nitrogen. Removal of the solvent molecules by drying and/or heating influences the phase transitions. With increasing temperature the strong Bragg peaks at 4.2, 9.3, 10.2 and 11.0° 2θ disappear and new maxima at 5.2 and 8.7° 2θ appear (see Fig. 7a and c). At a temperature of 320 °C in air, Cu_2O (PDF no. 5-667) and CuO (PDF no. 5-661) appear as new crystal phases. In a N_2 atmosphere, at the temperature of 550 °C, Cu (PDF no. 4-836) was detected.

Removal of the solvent by drying and/or heating the sample leads to structural changes (Fig. 5). This process is accompanied by the contraction of the crystal structure of **CFA-2** and a lack of permanent porosity. The structural

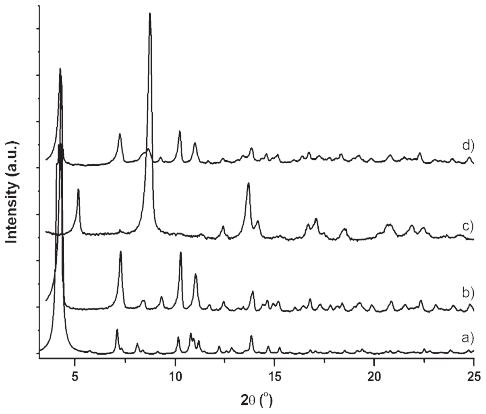

Fig. 5 XRPD measurements of **CFA-2**; calculated pattern (a); fresh sample (b); sample heated in vacuum (100 °C, 0.5 h) (c); dried sample re-solvated with DEF (d).

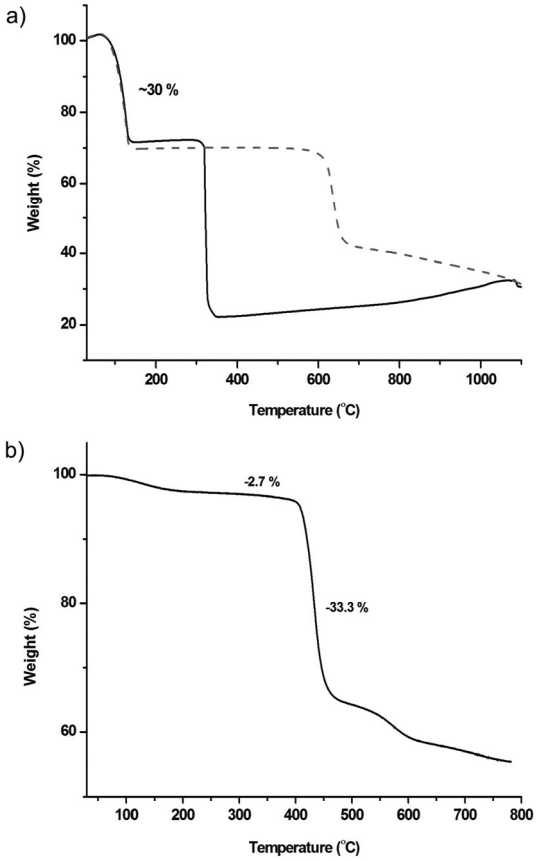

Fig. 6 Temperature dependent weight-loss of **CFA-2**, sample exposed to flowing nitrogen (dashed line) and oxygen gas (solid line) (a); temperature dependent weight-loss of **CFA-3**, sample exposed to flowing nitrogen (b).

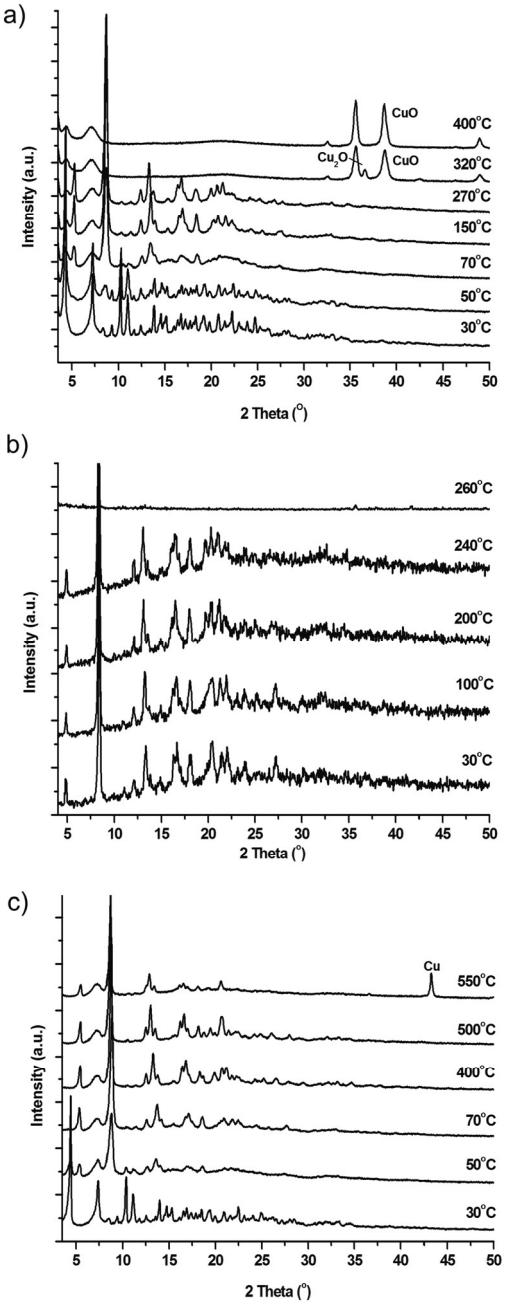

Fig. 7 VTXRPD plots of **CFA-2** under air (a), Cu – PDF No. 4-836; under oxygen (b) and under nitrogen (c), CuO – and Cu_2O – PDF No. 5-661 and 5-667, respectively. In the case of a measurement under oxygen, the sample was previously evacuated at room temperature.

changes caused by removal or uptake of solvent are described in the physisorption section.

Interestingly, the intensities of the lines can be recovered after the desolvated compound was taken up with solvents such as MeOH, EtOH, DEF or DMF, which indicates that the solvent removal is completely reversible and the initial structure can be recovered (Fig. 5). The breathing phenomenon is relatively fast (approx. 30 minutes). Mechanical stress originating from the structural transformations frequently leads to crystal fracture (see Fig. S4†). If **CFA-2** is immersed into benzene or chlorobenzene no uptake of solvents was observed.

In the case of **CFA-3** three decomposition steps were detected. The first one, in the temperature range of 30–270 °C, is connected with removal of solvent, the two next steps

between 270–550 °C and 550–800 °C correspond to the gradual pyrolitic decomposition of the compound. Variable temperature powder X-ray diffraction studies show (Fig. S5†) that the crystal structure of **CFA-3** is stable up to 300 °C. In the temperature range of 30–300 °C only small differences (peaks shift to lower 2θ values, approximately 0.2° 2θ) are observed. At a temperature of 350 °C new peaks at 37.9 and 43.8° 2θ appear which can be ascribed to the silver solid phase (PDF no. 1-1164). Subsequent heating leads to the complete decomposition of the sample, only the phase of metallic silver is observed.

Physisorption results

According to the calculations performed by the PLATON/SQUEEZE program,[20] the initial total potentially accessible void volume of **CFA-2** is 14625.6 Å^3 (0.65 cm^3 g^{-1}) which is about 52.5% of the unit cell volume (27 865 Å^3) for a probe radius of 1.68 Å, corresponding to the approximate van der Waals radius of Ar.[22] In the case of **CFA-2** simple heating at 100 °C for 0.5 h under vacuum produces a sample with very low BET surface area (9.4 m^2 g^{-1}), and the exchange of the DEF solvent with a more volatile solvent (EtOH) with subsequent heating at 100 °C for 0.5 h under vacuum results only in a small increase of surface area to about 36 m^2 g^{-1}. In order to enhance the porosity of **CFA-2**, supercritical[23] and freeze drying[24] procedures were applied. The freeze drying procedure (benzene) had no significant influence on the surface area. The supercritical drying (SCD) procedure, however, leads to much larger surface area (327 m^2 g^{-1}), approx. nine times bigger in comparison to solvent exchange and heating in vacuum. The argon adsorption isotherm after SCD follows type I behaviour, typical for microporous solids. The maximum uptake achieved at 77 K and p/p_0 = 1 is 125 cm^3 g^{-1} (Fig. 8). The micropore volume obtained from the sorption isotherm is 0.13 cm^3 g^{-1} using the NLDFT method.[25] The same value was obtained by using the de Boer t-method micropore analysis.[26] The adsorption data were fitted to the BET equation to give a surface area of 327 m^2 g^{-1}. This value is much smaller than the surface area calculated from a Monte Carlo technique (where a probe molecule is 'rolled' over the surface), which is 1914 m^2 g^{-1} based on the crystal data of the **CFA**-2-solvated form from single crystal analysis.[27]

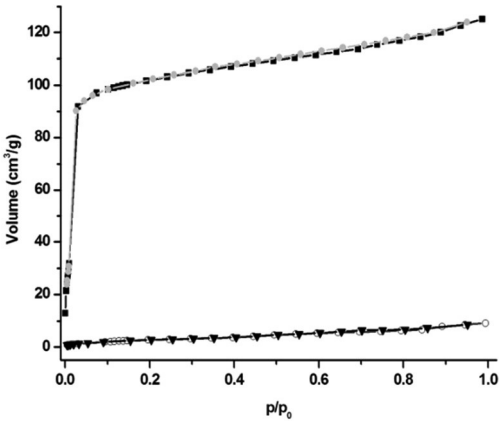

Fig. 8 Argon adsorption (black squares) and desorption (grey circles) isotherms measured for **CFA-2** after supercritical drying. Ar adsorption (black triangles) and desorption (open circles) isotherms for **CFA-2** evacuated at 100 °C for 1 h.

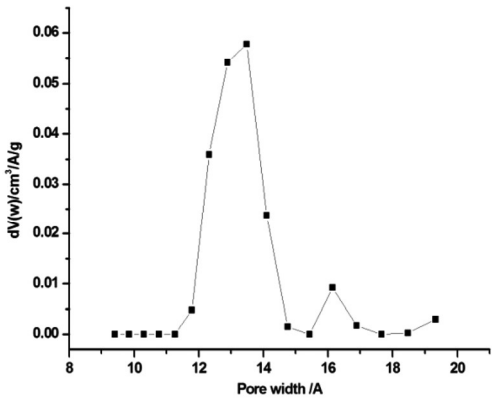

Fig. 9 Pore size distribution for **CFA-2** calculated by fitting the NLDFT model to the Ar adsorption data.

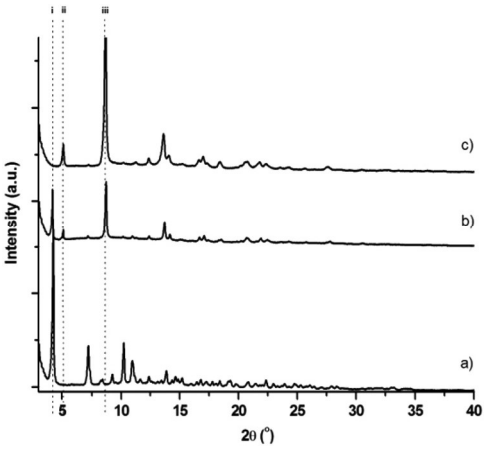

Fig. 10 XRPD patterns of freshly prepared Cu_2(phbpz)]·2DEF·MeOH (**CFA-2**) (a); [Cu_2(phbpz)] after supercritical drying (b); [Cu_2(phbpz)] after heating in vacuum at 100 °C for 0.5 h (c).

To evaluate the pore size distribution, the argon sorption isotherms sampled at 77 K were analyzed using non-local density functional theory (NLDFT) implementing a carbon equilibrium transition kernel for argon adsorption at 77 K based on a slit-pore mode.[28] The distribution calculated by fitting the adsorption data reveals micropores with the diameter in the range of 12–14.5 Å (Fig. 9) which is in good agreement with the data from crystal structure. Additionally, XRPD measurements were registered for samples evacuated at 100 °C and after the SCD procedure (Fig. 10).

The powder diffraction patterns were indexed and the results are collected in Table 2. According to the XRPD data, some of the characteristic peaks became weaker and disappeared and new peaks appeared in comparison to the fresh sample. Especially, the most intensive and characteristic peak

Table 2 Unit cell parameters for synthesized, dried by SCD and evacuated **CFA-2** samples

Compound	Space group	Unit cell parameters (Å)				Surface area ($m^2\ g^{-1}$)	
		$a = b$	c	$\alpha = \beta = \gamma$ (°)	Volume (Å^3)	Calcd	Measured
$[Cu_2(phbpz)]$·2DEF·MeOH	$I4_1/a$	30.835(14)	29.306(7)	90	27 865(19)	1914	
$[Cu_2(phbpz)]$ – after SCD	$I4_1/a$	34.900(2)	21.021(4)	90	25 603(3)		327
$[Cu_2(phbpz)]$ – evacuated at 100 °C 0.5 h	$I4_1/a$	34.905(3)	13.477(8)	90	16 419(3)		9.4

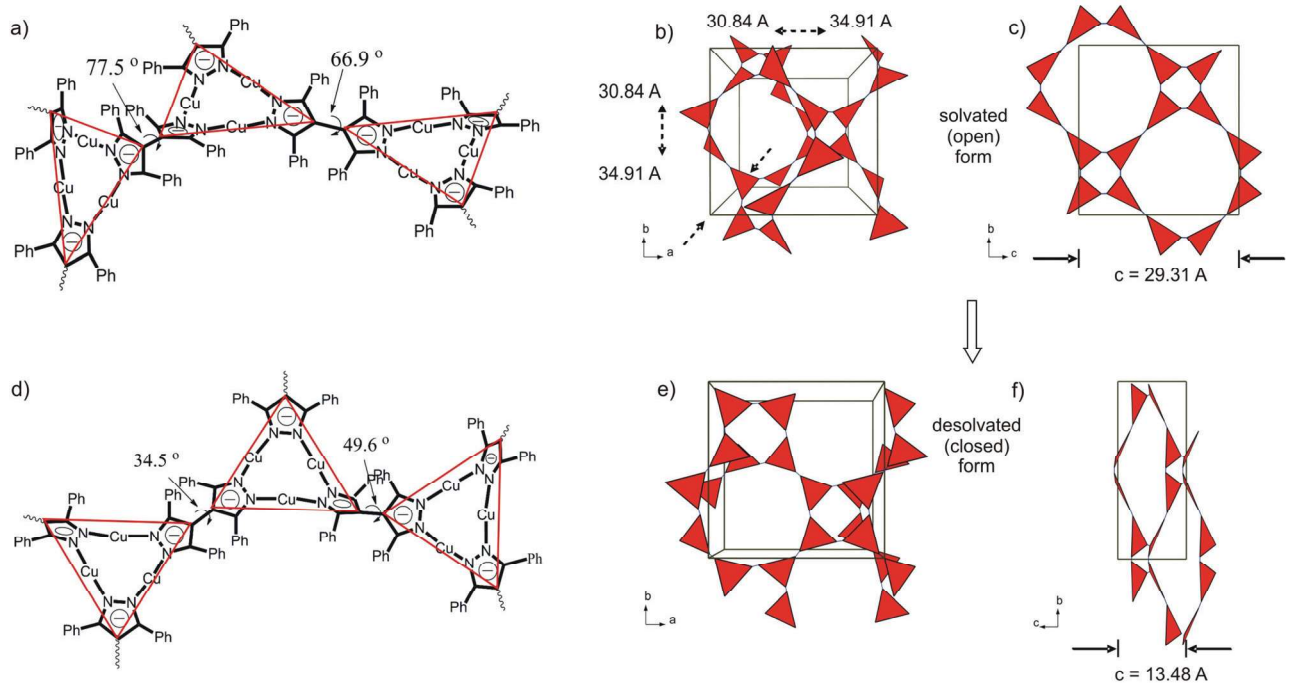

Fig. 11 Schematic drawing of connection of $\{Cu_3\}$ units in CFA-2 solvated (a) and desolvated states (b). Packing diagrams represented by interconnected SBUs of CFA-2 showing 3D frameworks projected along the *c*- (b) and *a*-axis (c), solvated state, (e) and (f) desolvated form, respectively.

at 4.2° 2θ, which corresponds to the (101) plane dividing in half the channels in the fresh sample, totally disappeared after drying the probe. It can be seen that after supercritical drying a mixed state of two phases is observed (the pore volume amounts to approx. 20% of the pore volume of fresh synthesized sample): there are maxima seen which are characteristic for the fresh sample (i) and for the evacuated sample (ii). Heating the probe and removal of the solvent have an enormous impact on the unit cell size changes (see Table 2). The structural model of **CFA-2** after solvent removal was gleaned from force-field calculations (Forcite force-field integrated in Accelrys Materials Studio, V6.0, restraining the unit cell dimensions to a = 34.905(3), c = 13.477(8)) as determined from the XRPD pattern of the desolvated sample by using the PROSZKI package.[29] The perfect match between the XRPD patterns of the evacuated **CFA-2** sample and the calculated model is observed (see ESI, Fig. S6†). The model exhibits a densely packed structure (Fig. 11), the total potentially accessible void volume is 581.7 Å^3 which is 3.5% of the unit cell volume (16 419(3) Å^3) for a probe radius of 1.68 Å.[23]

The structural transition from the solvated to the desolvated sample can be modeled without disrupting the existing covalent or coordinate bonds. It can be described as a dynamic distortion along the *c*-direction of the tetragonal lattice (from 29.306(7) Å in **CFA-2** to 13.477(9) Å) in the desolvated state, which is accompanied by a widening of the *a* lattice constant (from 30.835(14) Å to 34.905(3) Å) in the desolvated state. Removal of the solvent molecules causes a drastic volume change (*ca.* 59%).

Since the network topology is maintained during desolvation, the lattice changes are continuous and can be described by the angle between the planar Cu_3-$(pz)_3$ unit systems, which changes from 66.9(1)–77.5(1)° (solvated state) to 34.5(1)–49.6(1) (desolvated state) (see Fig. 11).

Note that this dynamic and reversible breathing transformation is also seen in the change of crystal morphology upon drying (compare Fig. 1), where the square pyramidal shape of the crystals shows a compression along the fourfold axis of crystal symmetry upon drying, which corresponds to the *c*-direction of the tetragonal crystal system.

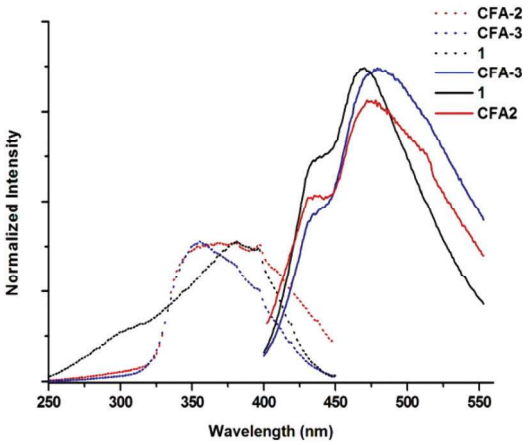

Fig. 12 Solid-state photoluminescence spectra for the compounds **1**, **CFA-2** and **CFA-3** at room temperature. Dashed-lines – excitation spectra, continuous-lines – emission spectra.

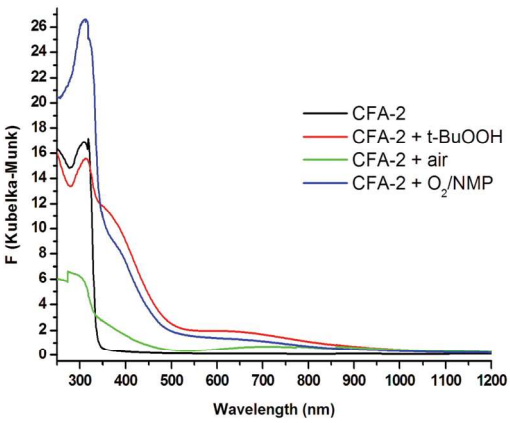

Fig. 13 UV-vis spectra of **CFA-2** at room temperature. Black line – **CFA-2** (freshly prepared and solvated), red – **CFA-2** oxidized by *t*-BuOOH, green – **CFA-2** after standing in the solution of EtOH under air over 2 months, **CFA-2** oxidized by oxygen in NMP solution.

Photoluminescence and UV-vis spectroscopy

Trinuclear d^{10} compounds have been utilized as luminescent materials.[30] Some complexes with Cu^{I} and Ag^{I} metal ions show very unusual near-infrared luminescence.[31] For polynuclear copper clusters, the Cu–Cu distance plays an important role in photoluminescence properties.[32] Normally the Cu–Cu distance must be less than or close to twice the van der Waals radius of Cu^{I} (1.4 Å) in order to achieve low-energy emission. Thus, the $Cu_4I_4py_4$ complex displaying a Cu–Cu distance of 2.69 Å shows a strong emission band at 615 nm in the solid state at 77 K, whereas $[CuIpy]_\infty$ with a Cu–Cu distance of 2.88 Å shows only one emission band at 449 nm.[33] Compounds **1**, **CFA-2** and **CFA-3**, irradiated at 381 nm (**1** and **CFA-2**) and 355 nm (**CFA-3**), give broad emission bands in the visible region with the maxima at 435 nm (**1**, **CFA-3**), 468 nm (**1**), 474 nm (**CFA-2**) and 478 nm (**CFA-3**) (Fig. 12). Thus, both compounds **CFA-2** and **CFA-3** show only a slight red shift of the emission band, as compared to a free ligand **1**. Obviously, the Cu–Cu distance in compound **CFA-2** (3.192(2)–3.263(1) Å) is too large to influence the luminescence properties and the emission is probably related to the π–π* transition of the aromatic ligand. Similarly, Ag–Ag interactions in compound **CFA-3** are not strong enough (the Ag–Ag distance lies in the range 3.31–3.7 Å, whereas the sum of van der Waals radii of the Ag^{+} ion is 3.4 Å) and do not affect the luminescence properties.

In order to prove the reactivity of **CFA-2** towards molecular oxygen, the sample was investigated with UV-vis spectroscopy. The solid-state UV-vis spectrum of **CFA-2** displays one strong absorption peak at 312 nm in the UV region which could be assigned to the intraligand electron transitions (Fig. 13). Adding an acetonitrile solution of *t*-BuOOH to **CFA-2** leads to green-coloured crystals, indicating an oxidation of Cu(I) ions to Cu(II) (see Fig. 14a–c). The UV-vis spectrum of the oxidized sample exhibits one additional broad peak with the maximum centered at 635 nm, which encompasses the Cu^{II} d–d transitions.[33] The oxidation of **CFA-2** in air is very slow and leads to a product with a very broad absorption band indicating that

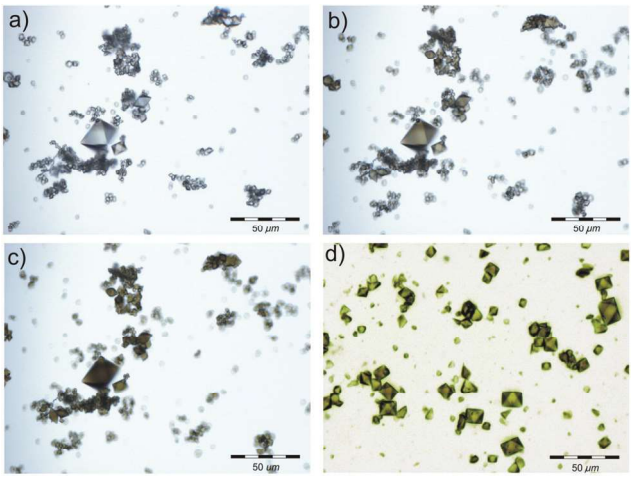

Fig. 14 Optical micrographs of **CFA-2** crystals oxidized by *t*-BuOOH (a–c). The images were recorded at time steps of 3 minutes after exposing crystals of **CFA-2** to a solution of *t*-BuOOH in DMF at c = 100 mmol L^{-1}. **CFA-2** crystals oxidized by oxygen in NMP (d).

probably different Cu(II) species were formed. However, bubbling pure oxygen gas through a solution of NMP (1-methyl-2-pyrrolidone) containing **CFA-2** leads to the fast oxidation of the sample and a color change to green (see Fig. 14d). The UV-vis spectrum is similar to the spectrum of **CFA-2** oxidized by *t*-BuOOH. Furthermore, the oxidized **CFA-2** sample can be reduced to a Cu(I) compound upon heating in DMF at 120 °C for 3–4 hours. The XRPD patterns of the oxidized as well as reduced samples are similar to the freshly prepared **CFA-2** (Fig. S7†), indicating that the structure remains stable during the oxidation/reduction sequence. This shows that **CFA-2** is a potential catalyst for the oxidation reactions in a liquid phase.

Unfortunately all attempts to collect X-ray diffraction data of oxidized single crystals of **CFA-2** as yet have failed in our hands, which is ascribed to the very weak scattering of the crystals.

Conclusions

The work reported here focuses on the synthesis and characterization of a novel metal–organic framework assembled from trinuclear Cu(I)/Ag(I) secondary building units (SBUs) and tetradentate 3,3′,5,5′-tetraphenyl-bipyrazolate ligands. From the crystal engineering point of view, the use of pyrazolato-based ligands comprising bulky substituents (*i.e.* phenyl) leads to MOFs that exhibit a reduced tendency for interpenetration (**CFA-2** is two-fold interpenetrated) as opposed to MOFs built from pyrazolato ligands containing CH_3 groups (eight- or four-fold interpenetrated). On the other hand, the steric influence of the phenyl substituents is still insufficient to prevent structural changes upon removal of the occluded solvent molecules.

CFA-2 accordingly exhibits large breathing effects upon exposure to different kinds of polar liquids (MeOH, EtOH, DMF, DEF), whereas non-polar solvents (benzene, naphthalene, tetralin (1,2,3,4-tetrahydronaphthalene)) are not taken up at all. The structural dynamics accompanying solvent uptake or removal in **CFA-2** can be described by a single structural parameter, namely the interplanar angle φ between the adjacent heterocyclic ring systems of the bipyrazole ligands, which changes from 66.9(1)–77.5(1)° (fully solvated state) to 34.5(1)–49.6(1) (fully desolvated state). Preliminary studies of **CFA-2** reactivity toward molecular oxygen show that this compound is stable during the oxidation and reduction sequence of Cu ions. **CFA-2** therefore is a potential catalyst for performing oxidation reactions in the liquid phase, albeit the high structural dynamics (*i.e.* swelling) of the lattice upon loading with different solvents will make the structural characterization of the activated and coordinated oxygen species a difficult task. Less flexible, robust MOFs containing trinuclear Cu(I) units might better serve the purpose of elucidating mechanistic details of oxygen activation, which are currently being developed.

Experimental

Materials and general methods

All reagents were of analytical grade and used as obtained from commercial sources without further purification. Fourier transform infrared (FTIR) spectra were recorded in the range of 4000–400 cm^{-1} on a Bruker Equinox 55 FT-IR spectrometer equipped with an ATR unit. The following indications are used to characterize absorption bands: very strong (vs), strong (s), medium (m), weak (w). NMR spectra were recorded on a Varian 400 NMR spectrometer; data given as ppm; spectra referenced to the residual solvent peak. Elemental analyses (C, H, N) were carried out on a Perkin-Elmer 2400 Elemental Analyzer. Thermogravimetric analysis (TGA) was performed with a TGA/SDTA851 Mettler Toledo analyzer in a temperature range of 25–1100 °C in flowing nitrogen or oxygen at a heating rate of 10 °C min^{-1}. Ambient temperature X-ray powder diffraction (XRPD) patterns were recorded either on a PANalytical X' Pert PRO diffractometer with an X'Celerator detector operated at 45 kV, 40 mA, Cu Kα (λ = 1.54178 Å) with a scan speed of 98.58 s per step and a step size of 0.033° in 2θ, or on a Seifert XRD 3003 TT diffractometer equipped with a Meteor1D detector operated at 40 kV, 40 mA, Cu Kα (λ = 1.54178 Å) with a scan speed of 10 s per step and a step size of 0.02° in 2θ. Variable temperature X-ray powder diffraction (VTXRPD) measurements were performed in air or in a pure nitrogen atmosphere at a temperature ranging from 30 to 550 °C with a PANalytical X' Pert PRO diffractometer equipped with an Anton Paar HTK 1200N reaction chamber. VTXRPD measurements in pure oxygen were performed with a Siemens D5000 diffractometer equipped with an Anton Paar HTK 900 reaction chamber. The patterns were recorded in the 3–50° 2θ range, with time 98.6 s per step, and a step 0.033° 2θ at different temperatures. Temperature program between measurements: heating rate 5 °C min^{-1}, then 10 min isotherm. Argon sorption isotherms at −196 °C up to p/p_0 = 1 were measured using a Quantachrome Autosorb-1C apparatus. High purity gas was used for the adsorption experiments (argon 99.999%). Luminescence spectra were acquired with a spectrofluorimeter (FS920 Edinburgh Instruments) equipped with a TMS300 monochromator, an S900 single photon photomultiplier, and a Xe900 450W xenon arc lamp at room temperature. The excitation and emission spectra were corrected for the wavelength-dependent lamp intensity and detector response, respectively. The UV-vis spectra were recorded on a Perkin-Elmer Lambda 750S spectrometer in the range of 250–2000 mm with a lamp change at 320 nm.

Synthesis of 3,3′,5,5′-tetraphenyl-1*H*,1′*H*-4,4′-bipyrazole (1)

Bipyrazole **1** was synthesized by a modified procedure.[19] To a solution of 15.00 g (29.90 mmol) di-potassium-3,3′-5,5′-tetraphenyl-1,1′-dihydroxy-4,4′-bipyrazol-2,2′-dioxide[34] in 600 mL glacial acetic acid, 45.00 g (688 mmol) zinc powder was added and the resulting suspension was heated to reflux. After completion of the reaction (monitored by TLC) the mixture was cooled to r.t. and filtered to remove the excess of zinc powder. The product, precipitated by slowly pouring the filtrate into 2 L of water, was filtered off and washed extensively with water to remove the remaining zinc salts. After drying pure bipyrazole **1** (6.14 g, 14.00 mmol; 46%) was obtained as a colorless solid. The compound is soluble in DMF, DEF, DMAc, 1,4-dioxane, DMSO, hot MeOH, EtOH and insoluble in H_2O, THF, chlorobenzene, nitrobenzene, CH_3CN. M.p. 120–130 °C; IR (cm^{-1}): 3068 (w), 1601 (w), 1493 (w), 1466 (w), 1447 (w), 1434 (w), 1393 (w), 1313 (w), 1291 (w), 1256 (w), 1178 (w), 1149 (w), 1092 (w), 1071 (w), 1025 (w), 1001 (w), 966 (m), 950 (m), 912 (s), 840 (vs), 783 (m), 764 (m), 740 (w), 711 (w), 689 (w), 592 (w), 536 (w), 509 (m), 453 (w), 412 (w). ^{1}H NMR (400 MHz, DMSO-d_6, 25 °C, ppm): 13.53 (s, 2 H), 7.44 (s_{br}, 8 H), 7.16–7.23 (m, 12 H); ^{1}H NMR (400 MHz, $CDCl_3$–MeOH-d_4 4 : 1, 25 °C, ppm): 7.26–7.44 (m, 8 H), 7.11–7.14 (m, 12 H); ^{13}C NMR (100 MHz, $CDCl_3$–MeOH-d_4 4 : 1, 25 °C, ppm): 147.2, 131.3, 128.2, 127.7, 126.8, 107.8. The IR, ^{1}H NMR and ^{13}C NMR spectra are shown in Fig. S8, S9 and S10,† respectively. MS (EI,

m/*z* (%)): 438 (8) [$M^{\cdot+}$], 353 (100), 352 (23), 235 (3), 234 (13), 231 (4). Elemental analysis for $C_{30}H_{22}N_4$: calcd C: 82.17; H: 5.06; N: 12.78 (%); found: C: 81.85; H: 5.39; N: 12.56 (%).

Synthesis of [Cu_2(phbpz)]·2DEF·MeOH (CFA-2)

Solvothermal method. In a typical procedure, a mixture of $Cu(OAc)_2{\cdot}H_2O$ (4 mg, 0.02 mmol) and 3,3′,5,5′-tetraphenyl-1*H*,1′*H*-4,4′-bipyrazole (15 mg, 0.034 mmol) was dissolved in a mixture of 2.5 mL DEF and 2.5 mL MeOH. To this mixture 0.1 mL of Et_3N was added and the solution was placed in a glass tube (10 mL). The tube was closed with a cap and heated up to 110 °C in 30 minutes and kept at this temperature for three days after which it was allowed to slowly cool down to room temperature. Colorless crystals were filtered off by suction, washed thoroughly with MeOH and stored under nitrogen. The synthesis can be similarly performed at larger quantities (upscale factor: 50). Elemental analysis for $Cu_2(C_{30}H_{20}N_4){\cdot}2(C_5H_{11}NO){\cdot}CH_3OH$: calcd: C: 61.71; H: 5.81; N: 10.53 (%); found: C: 61.14; H: 5.66; N: 10.96 (%). IR: (cm^{-1}): 1601 (w), 1465 (m), 1444 (m), 1417 (w), 1330 (w), 1319 (w), 1298 (w), 1271 (w), 1176 (w), 1109 (m), 1069 (w), 1009 (w), 960 (s), 907 (s), 835 (vs), 793 (s), 756 (s), 742 (m), 724 (m), 692 (w), 652 (w), 612 (w), 530 (w), 511 (w), 498 (w), 469 (w), 442 (w), 418 (w). The IR spectrum of **CFA-2** is shown in Fig. S8.†

Diffusion synthesis at room temperature. Colorless crystals of **CFA-2** were obtained by layering a solution of 3,3′,5,5′-tetraphenyl-1*H*,1′*H*-4,4′-bipyrazole (15 mg, 0.034 mmol) dissolved in 4 mL of EtOH on a solution of Cu_2O (4 mg, 0.028 mmol) dissolved in 1 mL of aqueous ammonia (28 weight%). The colorless crystalline material was washed with MeOH and stored under nitrogen. This material exhibits analytical results identical to those reported for the product from the solvothermal synthesis route.

Synthesis of [Ag_2(phbpz)] (CFA-3)

In a typical procedure a solution of 3,3′,5,5′-tetraphenyl-1*H*,1′*H*-4,4′-bipyrazole (15 mg, 0.034 mmol) dissolved in 4 mL of EtOH was layered on a solution of Ag_2O (4 mg, 0.017 mmol) in 1 mL of aqueous ammonia (28 weight%). After 5 days, colorless crystals appeared. The colorless crystalline material was washed with MeOH and dried in air at ambient conditions. The synthesis can be similarly performed at larger quantities (upscale factor: 50). Elemental analysis for $Ag_2(C_{30}H_{20}N_4)$: calcd: C: 55.24; H: 3.09; N: 8.59 (%); found: C: 55.31; H: 3.20; N: 8.46 (%); IR (cm^{-1}): 1603 (w), 1462 (w), 1443 (m), 1410 (w), 1328 (w), 1320 (w), 1295 (w), 1268 (w), 1172 (w), 1158 (w), 1106 (w), 1071 (w), 1030 (w), 1007 (w), 955 (w), 906 (w), 876 (w), 832 (w), 794 (w), 758 (s), 736 (m), 717 (m), 690 (vs), 646 (m), 616 (w), 603 (w), 589 (w), 520 (m), 497 (w), 473 (w), 451 (w), 425 (w), 410 (w). The IR spectrum for **CFA-3** is shown in Fig. S8.†

Single crystal X-ray diffraction

3,3′,5,5′-Tetraphenyl-1*H*,1′*H*-4,4′-bipyrazole·DMSO (1). **1** was recrystallized from DMSO and colorless needle-shaped crystals were obtained. X-ray data for the single crystal structure determination of **1** were collected on a Bruker D8 Venture diffractometer. A total of 1099 frames were collected. The frames were integrated with the Bruker SAINT software package using a narrow-frame algorithm. The integration of the data using a monoclinic unit cell yielded a total of 49 286 reflections to a maximum θ angle of 25.00° (0.84 Å resolution), of which 4863 were independent (average redundancy 10.135, completeness = 99.5 %, R_{int} = 5.30 %, R_{sig} = 2.44 %) and 4231 (87.00 %) were greater than $2\sigma(F^2)$. The final cell constants are a = 10.3718(12) Å, b = 16.0120(16) Å, c = 16.776(2) Å, β = 94.124(5)°, volume = 2778.8(5) $Å^3$. The calculated minimum and maximum transmission coefficients (based on crystal size) are 0.7110 and 0.7457. The structure was solved by direct methods and refined using SHELXS and SHELXL-97 programs,[35] respectively. The final anisotropic full-matrix least-squares refinement on F^2 with 407 variables converged at R_1 = 4.49 % for the observed data and wR_2 = 10.97 % for all data. The goodness-of-fit was 1.061. The largest peak in the final difference electron density synthesis was 0.570 e^- $Å^{-3}$ and the largest hole was −0.368 e^- $Å^{-3}$ with an RMS deviation of 0.046 e^- $Å^{-3}$. On the basis of the final model, the calculated density was 1.235 g cm^{-3} and F(000), 1088 e^-. Selected crystal data and details of the refinement for compound **1** are listed in Table 3.

[Cu_2(phbpz)]·2DEF·MeOH (CFA-2). X-ray data for the single crystal structure determination of **CFA-2** were collected on a Bruker D8 Venture diffractometer. The total exposure time was 52.85 hours. The frames were integrated with the Bruker SAINT software package using a narrow-frame algorithm. The

Table 3 Crystal data and structure refinement summary for compounds **1**, **CFA-2** and **-3**

Compound	**1**	**CFA-2**	**CFA-3**
Empirical formula	$C_{32}H_{28}N_4OS$	$C_{90}H_{60}Cu_6N_{12}$	$C_{90}H_{60}Ag_6N_{12}$
Formula	$C_{30}H_{22}N_4{\cdot}(CH_3)_2SO$	$Cu_3C_{45}H_{30}N_6$	$Ag_2C_{30}H_{20}N_4$
M_r	516.64	845.37	1956.76
T/K	100(2)	200(2)	293(2)
Crystal system	Monoclinic	Tetragonal	Monoclinic
Space group (no.)	$P2_1/n$ (no. 14)	$I4_1/a$ (no. 88)	$P2_1/c$ (no. 14)
a/Å	10.3718(12)	30.835(14)	16.3399(3)
b/Å	16.0120(16)	30.835(14)	32.7506(4)
c/Å	16.776(2)	29.306(7)	16.2624(3)
β/°	94.124(5)		107.382(2)
V/$Å^3$	2778.8(5)	27 865(19)	8305.3(2)
Z	4	16	4
D_c/g cm^{-3}	1.235	0.806	1.565
μ/mm^{-1}	0.148	1.235	1.438
F(000)	1088	6864	3863
θ Range/°	2.34–25.00	2.08–66.81	3.10–25.00
Refls. collected	49 286	120 701	52 721
Refls. unique	4863	12 341	14 520
R_{int}.	0.0530	0.0436	0.0338
R_1 ($I > 2\sigma(I)$)[a]	0.0449	0.0455	0.0513
wR_2 (all data)[b]	0.1097	0.1286	0.1318
GooF	1.061	1.067	1.090
Largest diff. peak and hole/ $Å^{-3}$	0.570 and −0.368	0.451 and −0.828	1.106 and −1.719

[a] $R_1 = \Sigma||F_0| - |F_c||/\Sigma|F_0|$. [b] $wR_2 = \Sigma[w(F_0^2 - F_c^2)^2]/\Sigma[w(F_0^2)^2]]^{1/2}$.

integration of the data using a tetragonal unit cell yielded a total of 120 701 reflections to a maximum θ angle of 66.81° (0.84 Å resolution), of which 12 341 were independent (average redundancy 9.795, completeness = 99.9%, R_{int} = 4.43%, R_{sig} = 2.19%) and 10 211 (82.63%) were greater than $2\sigma(F^2)$. The final cell constants of a = 30.835(14) Å, b = 30.835(14) Å, c = 29.306(7) Å, volume = 27 864(19) Å^3 are based upon the refinement of the *XYZ*-centroids of 9775 reflections above 20 $\sigma(I)$ with 7.079° < 2θ < 133.3°. Data were corrected for absorption effects using the multi-scan method (SADABS). The ratio of minimum to maximum apparent transmission was 0.791.

The structure was solved by direct methods and refined using SHELXS and SHELXL-97 programs,[36] using the space group $I41/a$, with Z = 16 for the formula unit, $C_{45}H_{30}Cu_3N_6$. Hydrogen atoms were added at idealized positions. H-atoms were given isotropic displacement parameters equal to 1.2 times the equivalent isotropic displacement parameter of the parent atom to which the H-atom is bound. The final anisotropic full-matrix least-squares refinement on F^2 with 487 variables converged at R_1 = 7.97% for the observed data and wR_2 = 27.61% for all data. The goodness-of-fit was 2.205. The highest residual electron density of 1.678 e$^-$ Å^3 was found in the large cavities of **CFA-2**, which is ascribed to the presence of heavily disordered solvent molecules. It was not possible to refine the positions of these molecules and, therefore, they were excluded from structure analysis by using the PLATON's SQUEEZE procedure.[20] The final anisotropic full-matrix least-squares refinement on F^2 with 487 variables converged at R_1 = 4.55% for the observed data and wR_2 = 12.86% for all data. The goodness-of-fit was 1.067. The largest peak in the final difference electron density synthesis was 0.451 e$^-$ Å^3 and the largest hole was −0.828 e$^-$ Å^{-3} with an RMS deviation of 0.060 e$^-$ Å^{-3}. On the basis of the final model, the calculated density was 0.806 g cm^{-3} and F(000), 6864 e$^-$. Selected crystal data and details of structure refinement for **CFA-2** are provided in Table 3.

[Ag$_2$(phbpz)] (CFA-3). X-ray data for the single crystal structure determination of **CFA-3** were collected on the Oxford Diffraction SuperNova four circle diffractometer, using a Mo Kα radiation source (λ = 0.71069 Å) and a graphite monochromator. Cell refinement and data reduction were performed using the CrysAlisPro program.[36] The positions of all of the non-hydrogen atoms were determined by direct methods using SIR-97.[37] All non-hydrogen atoms were refined anisotropically using weighted full-matrix least-squares on F^2. Refinement and further calculations were carried out using SHELXL-97.[36] All hydrogen atoms were placed at idealized positions and refined using a riding model with U_{iso}(H) fixed at 1.2U_{eq} of the parent C atom. Selected crystal data and the refinement details for the compound **CFA-3** are listed in Table 3.

Complete crystallographic data for the structures **1**, **CFA-2** and **-3** reported in this paper have been deposited in the CIF format with the Cambridge Crystallographic Data Center as supplementary publication no. CCDC 903114–903116.

Acknowledgements

This work was supported by a grant from the Ministry of Science, Research and Art Baden-Wuerttemberg and by the German Research Foundation (DFG) within Priority Program "Porous Metal–Organic Frameworks" (SPP 1362, MOFs). The authors thank Alexandre Santos Abreu (Augsburg University) for performing photoluminescence measurements.

Notes and references

1 (*a*) Ch. Banglin, X. Shengchang and Q. Guodong, *Acc. Chem. Res.*, 2010, **43**, 1115; (*b*) A. Dailly and E. Poirier, *Energy Environ. Sci.*, 2011, **4**, 3527; (*c*) L. J. Murray, M. Dincă and J. R. Long, *Chem. Soc. Rev.*, 2009, **38**, 1294.

2 (*a*) S. Qiu and G. Zhu, *Coord. Chem. Rev.*, 2009, **253**, 2891; (*b*) A. U. Czaja, N. Trukhan and U. Müller, *Chem. Soc. Rev.*, 2009, **38**, 1284; (*c*) J. R. Li, R. J. Kuppler and H. C. Zhou, *Chem. Soc. Rev.*, 2009, **38**, 1477; (*d*) E. Q. Procopio, F. Linares, C. Montoro, V. Colombo, A. Maspero, E. Barea and J. A. R. Navarro, *Angew. Chem., Int. Ed.*, 2010, **49**, 7308.

3 (*a*) S. Keskin and S. Kizilel, *Ind. Eng. Chem. Res.*, 2011, **50**, 1799; (*b*) E. Q. Procopio, S. Rojas, N. M. Padial, S. Galli, N. Masciocchi, F. Linares, D. Miguel, J. E. Oltra, J. A. R. Navarro and E. Barea, *Chem. Commun.*, 2011, **47**, 11751; (*c*) P. Horcajada, C. Serre, M. Vallet-Regi, M. Sebban, F. Taulelle and G. Férey, *Angew. Chem., Int. Ed.*, 2006, **45**, 5974; (*d*) R. C. Huxford, J. D. Rocca and W. Lin, *Curr. Opin. Chem. Biol.*, 2010, **14**, 262; (*e*) P. Horcajada, C. Serre, G. Maurin, N. A. Ramsahye, F. Balas, M. Vallet-Regí, M. Sebban, F. Taulelle and G. Férey, *J. Am. Chem. Soc.*, 2008, **130**, 6774; (*f*) J. An, S. J. Geib and N. L. Rosi, *J. Am. Chem. Soc.*, 2009, **131**, 8376.

4 (*a*) C. Sanchez, B. Julián, P. Belleville and M. Popall, *J. Mater. Chem.*, 2005, **15**, 3559; (*b*) O. Shekhah, J. Liu, R. A. Fischer and C. Wöll, *Chem. Soc. Rev.*, 2011, **40**, 1081; (*c*) B. V. Harbuzaru, A. Corma, F. Rey, J. L. Jorda, D. Ananias, L. D. Carlos and J. Rocha, *Angew. Chem., Int. Ed.*, 2009, **48**, 6476.

5 (*a*) S. T. Meek, J. A. Greathouse and M. D. Allendorf, *Adv. Mater.*, 2011, **23**, 249; (*b*) J. Y. Lee, O. K. Farha, J. Roberts, K. A. Scheidt, S. B. T. Nguyen and J. T. Hupp, *Chem. Soc. Rev.*, 2009, **38**, 1450; (*c*) M. Tonigold, Y. Lu, A. Mavrandonakis, A. Puls, R. Staudt, J. Möllmer, J. Sauer and D. Volkmer, *Chem.–Eur. J.*, 2011, **17**, 8671.

6 (*a*) A. Dhakshinamoorthy, M. Alvaro and H. García, *Catal. Sci. Technol.*, 2011, **1**, 856; (*b*) A. Corma, H. García and F. X. Llabrés i Xamena, *Chem. Rev.*, 2010, **110**, 4606.

7 (*a*) C. D. Wu, A. Hu, L. Zhang and W. Lin, *J. Am. Chem. Soc.*, 2005, **127**, 8940; (*b*) L. Ma, C. Abney and W. Lin, *Chem. Soc. Rev.*, 2009, **38**, 1248; (*c*) D. Dang, P. Wu, C. He, Z. Xie and C. Duan, *J. Am. Chem. Soc.*, 2010, **132**, 14321.

8 E. I. Solomon, U. M. Sundaram and T. E. Machonkin, *Chem. Rev.*, 1996, **96**, 2563.

9 L. Jian, C. Chen, F. Lan, S. Deng, W. Xiao and N. Zhang, *Solid State Sci.*, 2011, **13**, 1127.

10 D. Jiang, T. Mallat, F. Krumeich and A. Baiker, *J. Catal.*, 2008, **275**, 390.

11 D. Jiang, T. Mallat, D. M. Meier, A. Urakawa and A. Baiker, *J. Catal.*, 2010, **270**, 26.

12 (*a*) S. Marx, W. Kleist and A. Baiker, *J. Catal.*, 2011, **281**, 76; (*b*) F. X. Llabres i Xamena, O. Casanova, R. Galiasso Tailleur, H. Garcia and A. Corma, *J. Catal.*, 2008, **255**, 220.

13 D. Jiang, A. Urakawa, M. Yulikov, T. Mallat, G. Jeschke and A. Baiker, *Chem.–Eur. J.*, 2009, **15**, 12255.

14 V. Colombo, S. Galli, H. J. Choi, G. D. Han, A. Maspero, G. Palmisano, N. Masciocchic and J. R. Long, *Chem. Sci.*, 2011, **2**, 1311.

15 (*a*) A. A. Mohamed, *Coord. Chem. Rev.*, 2010, **254**, 1918; (*b*) H. V. R. Dias, H. V. K. Diyabalanage, M. G. Eldabaja, O. Elbjeirami, M. A. Rawashdeh-Omary and M. A. Omary, *J. Am. Chem. Soc.*, 2005, **127**, 7489; (*c*) H. V. R. Dias and H. V. K. Diyabalanage, *Polyhedron*, 2006, **25**, 1655; (*d*) M. Casarin, C. Corvaja, C. di Nicola, D. Falcomer, L. Franco, M. Monari, L. Pandolfo, C. Pettinari, F. Piccinelli and P. Tagliatesta, *Inorg. Chem.*, 2004, **43**, 5865; (*e*) S. M. Tekarli, T. R. Cundari and M. A. Omary, *J. Am. Chem. Soc.*, 2008, **130**, 1669.

16 (*a*) J. P. Zhang and S. Kitagawa, *J. Am. Chem. Soc.*, 2008, **130**, 907; (*b*) J. P. Zhang, S. Horike and S. Kitagawa, *Angew. Chem., Int. Ed.*, 2007, **46**, 889; (*c*) J. He, Y.-G. Yin, T. Wu, D. Li and X.-C. Huang, *Chem. Commun.*, 2006, 2845.

17 S. Maji, J. C.-M. Lee, Y.-J. Lu, C.-Li. Chen, M.-C. Hung, P. P.-Y. Chen, S. S.-F. Yu and S. I. Chan, *Chem.–Eur. J.*, 2012, **18**, 3955.

18 J.-R. Li, R. J. Kuppler and H.-C. Zhou, *Chem. Soc. Rev.*, 2009, **38**, 1477.

19 J. P. Freeman and J. F. Hansen, *J. Chem. Soc., Chem. Commun.*, 1972, 961.

20 PLATON/SQUEEZE program,A. L. Spek, *Acta Crystallogr.*, 2009, **65**, 148.

21 (*a*) A. A. Mohamed, L. M. Perez and J. P. Fackler, *Inorg. Chim. Acta*, 2005, **358**, 1657; (*b*) H. H. Murray, R. G. Raptis and J. P. Fackler, *Inorg. Chem.*, 1988, **27**, 26.

22 *Quantachrome Autosorb, Version 1.56*, 2009.

23 (*a*) A. I. Cooper and M. J. Rosseinsky, *Nat. Chem.*, 2009, **1**, 26; (*b*) M. Bouchaour, N. Diaf, A. Ould-Abbas, M. Benosman, L. Merad and N.-E. Chabane-Sari, *Rev. Energ. Ren.*, 2003, 99, ICPWE; (*c*) H. Furukawa, N. Ko, Y. Bok Go, N. Aratani, S. Beom Choi, E. Choi, A. Ö. Yazaydin, R. Q. Snurr, M. O'Keeffe, J. Kim and O. M. Yaghi, *Science*, 2010, **329**, 424.

24 L. Ma, A. Jin, Z. Xie and W. Lin, *Angew. Chem., Int. Ed.*, 2009, **48**, 9905.

25 P. I. Ravikovitch and A. V. Neimark, *Colloids Surf.*, 2001, **187**, 11.

26 F. Rouquerol, J. Rouquerol and K. Sing, in *Adsorption by Powders & Porous Solids*, Academic Press, San Diego, 1999.

27 (*a*) T. Düren, F. Millange, G. Férey, K. S. Walton and R. Q. Snurr, *J. Phys. Chem.*, 2007, **111**, 15350; (*b*) K. S. Walton and R. Q. Snurr, *J. Am. Chem. Soc.*, 2007, **129**, 1578.

28 J. Jagiello and M. Thommes, *Carbon*, 2004, **42**, 1227.

29 W. Lasocha and K. Lewinski, *J. Appl. Crystallogr.*, 1994, **27**, 437.

30 H. V. R. Dias, H. V. K. Diyabalanage, M. A. Rawashdeh-Omary, M. F. Franzman and M. A. Omary, *J. Am. Chem. Soc.*, 2003, **125**, 12072.

31 C. Yue, C. Yan, R. Feng, M. Wu, L. Chen, F. Jiang and M. Hong, *Inorg. Chem.*, 2009, **48**, 2873.

32 P. C. Ford, E. Cariati and J. Burassa, *Chem. Rev.*, 1999, **99**, 3625.

33 (*a*) F. G. Mutti, M. Gullotti, L. Casella, L. Santagostini, R. Pagliarin, K. K. Andersson, M. F. Iozzi and G. Zoppellaro, *Dalton Trans.*, 2011, **40**, 5436; (*b*) C. Di Nicola, Y. Y. Karabach, A. M. Kirillov, M. Monari, L. Pandolfo, C. Pettinari and A. J. L. Pombeiro, *Inorg. Chem.*, 2007, **46**, 221.

34 G. R. Stevenson, J. F. Hansen, G. Clark and J. P. Freeman, *J. Org. Chem.*, 1979, **44**, 3211.

35 G. M. Sheldrick, *SHELXL-97, Program for Refinement of Crystal Structures*, University of Göttingen, Germany, 1997.

36 Oxford Diffraction. *CrysAlis PRO*, Oxford Diffraction Ltd, Yarnton, England, 2010.

37 A. Altomare, M. C. Burla, M. Camalli, G. L. Cascarano, C. Giacovazzo, A. Guagliardi, A. G. G. Moliterni, G. Polidori, R. Spagna, *J. Appl. Crystallogr*, 1999, **32**, 115.